HIGH FIDELITY SIMULATION OF A DRONE PROPELLER IN HOVER

Alexis Dorange, Christophe Benoit, Eric Garnier, Stéphanie Péron
alexis.dorange@onera.fr,christophe.benoit@onera.fr,
eric.garnier@onera.fr,stephanie.peron@onera.fr
ONERA (France)

1 Context and motivations

Even though drones were initially developed for military purposes during World War I, they are now being widely used due to their large range of applications. Technological improvements enabled their use for many private and professional applications. Although drones have been widely studied in the field of flight control, their aerodynamic behavior is yet to be completely understood. Recently, some aerodynamic and aeroacoustic studies have been performed and published using Computational Fluid Dynamics (CFD) methods. Among these, some simulations use Reynolds-Averaged Navier-Stokes (RANS) models and others Large Eddy Simulation (LES) models[1] and they tend to rely on 3D scanned geometries of commercial propellers. There are plenty of drones flying around the world (the US Federal Aviation Administration has registered 865 thousands of drones across the US in May 2022) and a lot of manufacturers. However, limited information on the aerodynamics of industrial propellers can be found.

The vehicle that can be related to drones is the helicopter. More and more helicopter manufacturers are trying to build flying multi rotors taxis that resemble drones, for instance CityAirbus. But helicopter's rotors can not be simulated using high fidelity tools given their size and the fluid conditions. With a much smaller propeller such as a mini-drone's one, high fidelity computations seem realisable and may provide some important information regarding their performances.

This study aims at providing a better understanding of how a drone propeller behaves in hover. In this paper we will provide a fully described airfoil and propeller of a drone. An hybrid RANS/LES and a LES computations will be described and compared in an attempt to understand the physics of flight.

2 Methodology

2.1 Turbulence modelling

In this article, high-fidelity CFD computations of a drone with dual blades propeller in hover will be conducted. First, hybrid RANS/LES simulations are performed in order to determine the full LES mesh characteristics in terms of cell count and local mesh spacing. Finally, full LES simulation is performed on this mesh and analyzed. The hybrid RANS/LES method consists in solving the curvilinear mesh with a RANS model and the Cartesian mesh with a LES model. RANS simulations are achieved with the Spalart-Allmaras turbulence model[2], whereas the MILES approach[3] is used for the LES simulations.

2.2 Space and time discretization

In order to spatially discretize the Navier-Stokes equations a finite volume approach is pursued and a modified Advection Upstream Splitting Method (AUSM) scheme is used. The original AUSM was first introduced by Liou and Steffen[4] and was adapted for low Mach number flows. The AUSM+(P) model was introduced by Edwards and Liou[5] as a derivative of the first one, but provides a better coupling between pressure and velocity as well as being able to solve numerous flow regimes. In the full LES simulations, the

hybrid centered/upwind AUSM scheme introduced by Mary and Sagaut[6] called "sensor" and designed to reduce the numerical dissipation will be used. The time integration is achieved using a Newton LU-SGS implicit scheme[7].

2.3 Mesh topology

In our applications, blades are meshed with O-type near-wall multi-block structured grids and the remaining computational domain with a Cartesian grid or a set of Cartesian grids[8] as described in Figure 1.

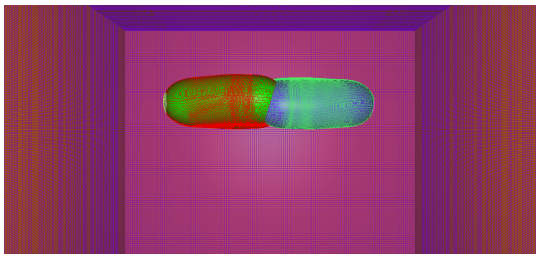

Figure 1: Mesh topology of the case.

Coupling between near-body meshes around each blade and the Cartesian mesh is performed through Chimera interpolations[9] to transfer the solution. Chimera transfers are achieved either at the external border of the near-body curvilinear grids or at the fringe of blanked points within the Cartesian mesh at each subiteration of the CFD solver. The off-body Cartesian mesh is built automatically and ensures a sufficient overlap and a cell spacing consistent with the near-body grids in the vicinity of the Chimera transfers[10]. It ensures the interpolation error to be of the same order of magnitude as the numerical error of the spatial discretization scheme.

With the previous technical choices, where the number of points of the Cartesian mesh is more important compared to the near-body mesh, the solver can be made very efficient: first, the computation of fluxes can be simplified on Cartesian grids, leading to less memory and CPU time requirements. In addition, the donor cell search routine used in Chimera is also dramatically simplified. Finally, the Cartesian mesh generation can be performed automatically in parallel.

2.4 Definition of quantities

The molecular viscosity is defined by the Sutherland law, which can be written in the form:

$$\mu = \mu_s \sqrt{\frac{T}{T_s}} \frac{1 + C_s/T_s}{1 + C_s/T} \ , \tag{1}$$

where T is the temperature, T_s is the constant Sutherland Temperature, C_s is the Sutherland constant depending on the nature of the gas and μ_s is a the Sutherland viscosity constant that depends on T.

In the one equation Spalart-Allmaras model the eddy viscosity μ_t is defined by:

$$\mu_t = \rho \widetilde{\nu} f_{v1} \ , \ f_{v1} = \frac{\kappa^3}{\kappa^3 + C_{v1}^3} \ , \ \kappa = \frac{\rho \widetilde{\nu}}{\mu} \ , \tag{2}$$

where ρ is the density, $\widetilde{\nu}$ is the kinematic viscosity transform, $C_{v1} = 7.1$ is a constant, and μ is the molecular viscosity as defined before.

The thrust is computed and is equal to:

$$T = \frac{1}{2} \rho V^2 S C_T \ , \tag{3}$$

where ρ is the density, $V = \Omega R$ is the velocity of the fluid, S is the contact surface and C_T is the thrust coefficient.

The Q criterion [11],[12] is one of the most widely used criterion for describing flow structures and it defined by:

$$Q = \frac{1}{2} \left(||\mathbf{\Omega}||^2 - ||\mathbf{S}||^2 \right) \ , \tag{4}$$

where $\mathbf{S}$ and $\mathbf{\Omega}$ are the symmetric and antisymmetric components of ∇u.

We also use the λ_2 criterion defined by Jeong and Hussain [13] which is defined by as the the second largest eigenvalue of $\mathbf{\Omega}^2 + \mathbf{S}^2$.

3 Definition of the blade geometry and test case conditions

3.1 Blade profile

The airfoil used in this paper is derived from the GEMFAN 5030R drone propeller but redefined as shown in Figure 2. The leading edge and trailing edge are both circles. The upper surface is a spline between the two circle edges and passing through the maximum thickness at mid chord. In a canonic definition of the airfoil, meaning that the leading edge is defined at $x = 0$ and the trailing edge at $x = 1$, the radius is $R = e/6$ with the thickness $e = 6/71$.

Figure 2: Definition of the airfoil.

3.2 Definition of the blade

The blade is defined using the previously defined airfoil and following the chord, twist, and dihedral distribution described in the Figures 3, 4, and 5. The equations for each distribution are given in a canonic form with $x = r/R$. The chord distribution is given by:

$$\begin{aligned} c(x) = &-640.95x^6 + 1951.1x^5 - 2295x^4 \\ &+ 1303.2x^3 - 379.16x^2 + 54.328x \\ &+ 10.829 \ , \end{aligned} \tag{5}$$

The twist distribution is given by:

$$\begin{aligned} t(x) = &-184.24x^6 + 434.5x^5 - 248.9x^4 \\ &- 73.559x^3 + 57.909x^2 + 4.8395x \\ &+ 17.888 \ , \end{aligned} \tag{6}$$

The dihedral angle distribution is given by:

$$d(x) = 0.5844x^2 - 4.4126x^2 + 2.385x + 0.8872 \ , \tag{7}$$

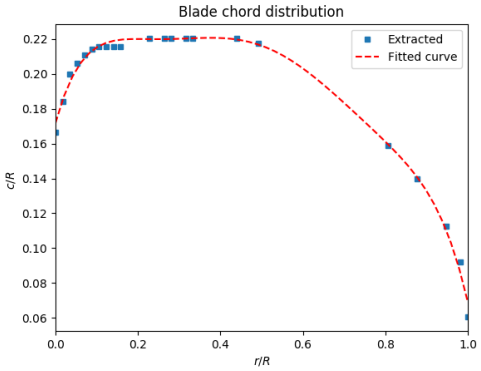

Figure 3: Chord distribution of the blade.

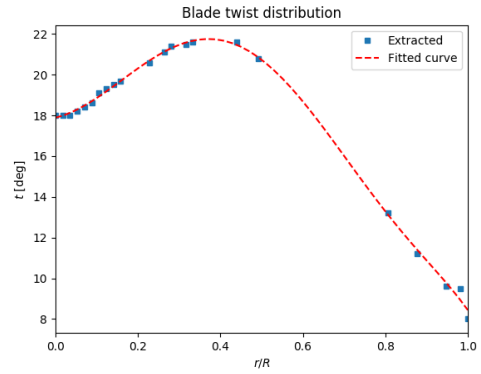

Figure 4: Twist angle definition of the blade.

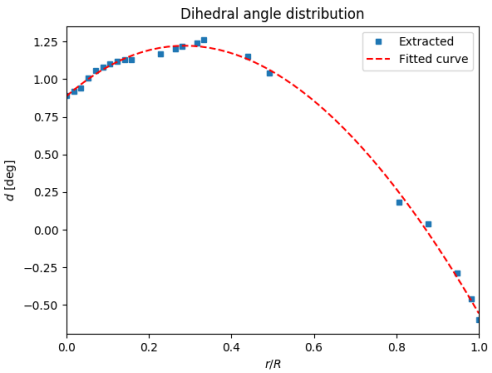

Figure 5: Dihedral angle definition of the blade.

Figure 6 yields the difference between the blade obtained by the scan and the blade obtained with the interpolation laws. The difference is not important as the average distance between both is equal to 0.25 mm and the maximum distance is equal to 0.5 mm. In the following chapters and computations we will consider only the interpolated blade.

Figure 6: Upper (right) and lower (left) surfaces of the blade obtained with scanned points (blue) and interpolated laws (red).

The propeller is obtained by considering two of the aforementioned blade and rotating one by 180° around the propeller rotation axis. It will be simulated without the central hub, as displayed in Figure 7.

Figure 7: Studied drone propeller configuration.

3.3 Flow conditions

The flow is defined by the following conditions:

$$Re_{tip} = 98,000 \ ; \ M_{tip} = 0.07 \ ;$$

$$R = 0.063 \ m \ ; \ \Omega = 377 \ rad/s \ ,$$

where Re_{tip} is the Reynolds number at the tip of the blade, M_{tip} is the Mach number at the tip of the blade, R is the radius of the blade, and Ω is the rotational speed of the propeller. These flow conditions are quite unusual compared to helicopter rotors and may be not adapted for RANS model due to the low Reynolds number.

4 RANS/LES simulations

4.1 Mesh and computation settings

The Cartesian mesh is designed such that 4 points are located within the main vortex core, corresponding to a minimum spacing of $10^{-3}m$. This resolution yields a mesh with 157 million points. The extent and the size of the blade grids are driven by the fact that the cell size at the fringe of the interpolated grids has to be similar to the local Cartesian cells. The resulting height of the outer cells of the curvilinear grids is $10^{-3}m$. Moreover the height of the first cell near the wall is set to $1.83 \times 10^{-6}m$ such that the dimensionless wall distance y^+ is equal to 1 for the first cell. The resulting curvilinear blade mesh is composed of 2.1 million points, giving a total mesh composed of 161 million points. At the border of the two meshes the eddy viscosity was found to be $\widetilde{\nu} \approx 0$ thereby allowing an accurate RANS/LES coupling. This case is run with a time step that corresponds to a variation of azimuth per iteration of $\Delta\psi = 0.25^{\circ}$. The simulation is computed with Roe's scheme on the curvilinear meshes and the sensor scheme on the Cartesian mesh.

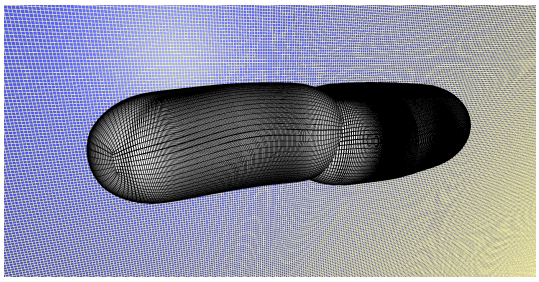

Figure 8: View of the hybrid RANS/LES mesh.

4.2 Results

Figure 9 displays the Q criterion ($Q = 400,000$) and Figure 10 the λ_2 criterion for the RANS/LES simulation after 17 revolutions.

Figure 9: Q criterion for RANS/LES.

Figure 10: λ_2 criterion for RANS/LES.

The vorticity magnitude is displayed on a cut plane along the rotation axis in Figure 11, highlighting strong vortices close the rotor, which are well-preserved and interacting downward after several revolutions.

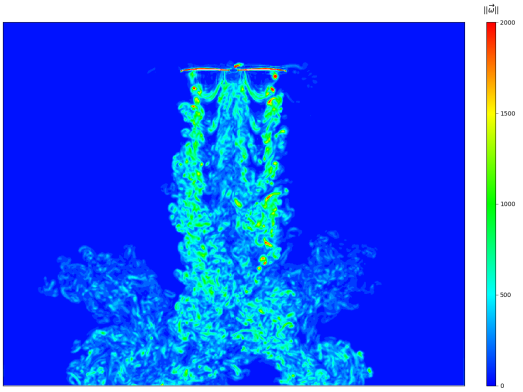

Figure 11: Vorticity for RANS/LES in a slice at at the center of the blade.

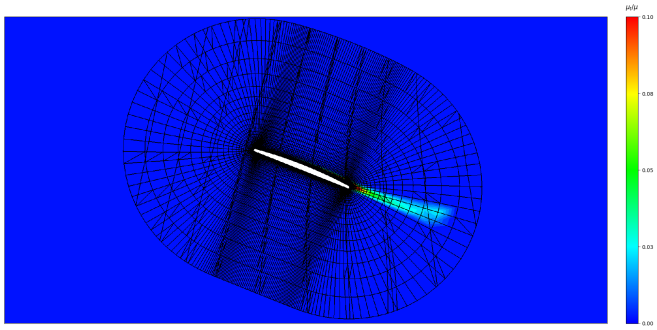

Figure 12: μ_T/μ slice at $r/R = 40\%$ with mesh.

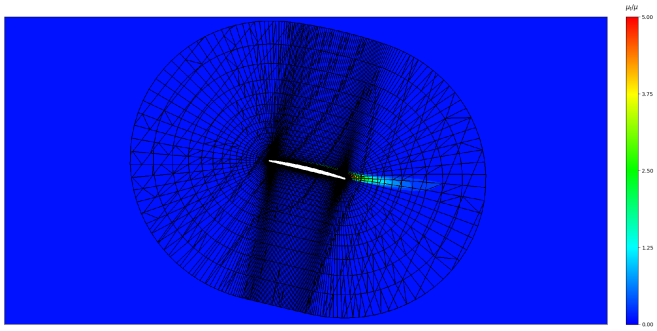

Figure 13: μ_T/μ slice at $r/R = 80\%$ with mesh.

The last two Figures 12 and 13 highlight that the curvilinear mesh is correctly implemented for a correct RANS/LES coupling since the turbulent viscosity is equal to zero before the junction between the curvilinear and the Cartesian mesh.

The low values of $\frac{\mu_t}{\mu}$ for $r/R = 40\%$ shows that the flow is almost entirely laminar and the turbulent boundary layer for $r/R = 80\%$ also results in low values of $\frac{\mu_t}{\mu}$.

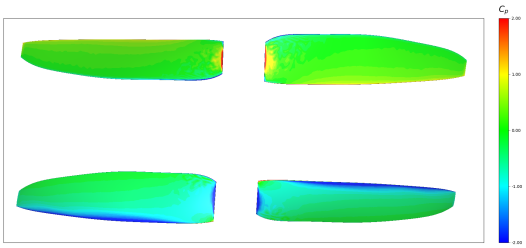

Figure 14: C_p map on the blade for RANS/LES.

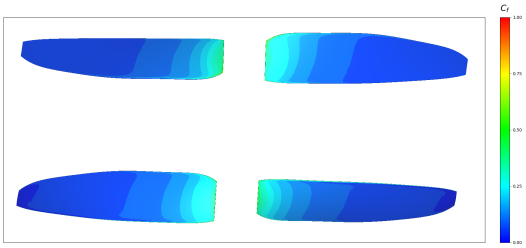

Figure 15: C_f map on the blade for RANS/LES.

The skin pressure coefficient C_p and friction coefficient C_f distributions are computed. They confirm the laminar behavior of the flow field (Figures 14 and 15). They also highlight the re-circulation part of the flow due to the lack of hub on the propeller.

5 Full LES mesh

The RANS/LES simulations enable the calculation of the vorticity thickness in the wake of the blade:

$$\delta_\omega = \frac{u_2 - u_1}{(\partial u/\partial y)_{max}}, \tag{8}$$

where u_2 and u_1 are the values of the velocity magnitude at two different locations in the wake of the blade, one above and one below that provide the maximum gradient.

To resolve the wake in the full LES simulation, the cell spacing is set to $\delta_\omega/2$ in the wake region in both the spanwise and streamwise directions. The mesh has to satisfy the $y^+ = 1$ condition while the streamwise and spanwise wall distances are set to $x^+ = 27$ and $z^+ = 10$ at the tip of the wing in the rotating frame, as suggested by Laurent et al.[14]. These conditions give $\Delta y = 2.43 \times 10^{-6} m$, $\Delta x = 6.58 \times 10^{-5} m$, and $\Delta z = 2.43 \times 10^{-5} m$. The curvilinear's last cell height is set to be equal to the Cartesian minimum cell spacing. This results in 85 million points in both curvilinear meshes.

In the Cartesian mesh, the main vortex, created at the tip of the blade, has to be accurately resolved. To fulfill this condition 10 points have to be located in its core. This corresponds to a minimum spacing of $4 \times 10^{-4} m$, which results in 2.4 billion points in the Cartesian mesh. The refinement to satisfy the vorticity thickness is realized after that. As in the farfield spanwise direction a fine resolution is not needed the mesh can be coarsened to have less points.

These settings lead actually to a huge number of points that would require a very high computational time; therefore, for a better compromise between computational time and the fidelity of the solution, the number of points in the vortex core has been reduced to 7 and z^+ value on the blade has been increased to 20. In order to increase the x^+ condition without modifying the geometry near the leading and trailing edges, a tangential law was used to discretize the airfoil, it gives Figure 16.

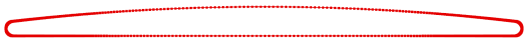

Figure 16: Airfoil for full LES mesh.

This leads to 57 million points for each curvilinear mesh and 500 million points for the Cartesian mesh, resulting in Figure 17. The computational time is calculated to have a CFL ≈ 1 for all the grids. It gives a time step that corresponds to an angle step of $\Delta\psi = 0.025^\circ$. The simulation is performed with the AUSM+(P) scheme on the curvilinear meshes and the sensor scheme on the Cartesian mesh. The LES simulation computes the fluctuating part of every quantities in addition to the time-averaged part. In order to compare with the hybrid RANS/LES simulation, time-averaged part of quantities

needs also to be extracted. The solution is averaged by phases of 10° in our case.

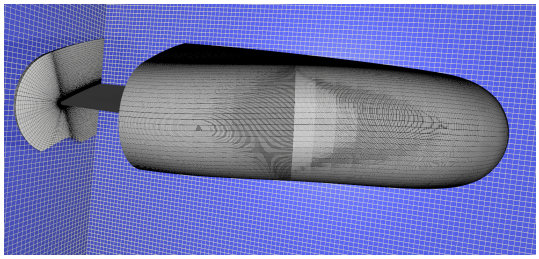

Figure 17: View of the full LES mesh.

Figure 19: λ_2 criterion for full LES.

5.1 Results

Figure 18 displays the Q criterion ($Q = 1$ million) and Figure 19 the λ_2 criterion for the full LES simulation after 9 revolutions.

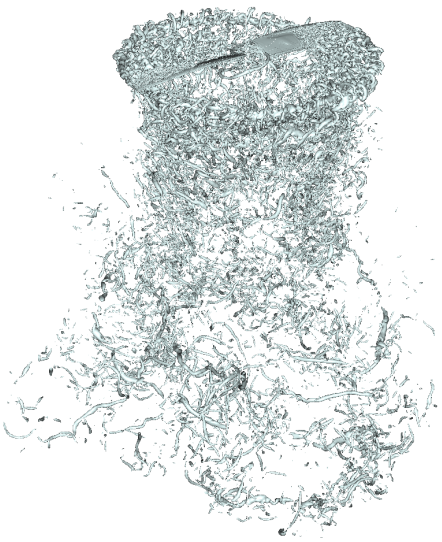

Figure 18: Q criterion for full LES.

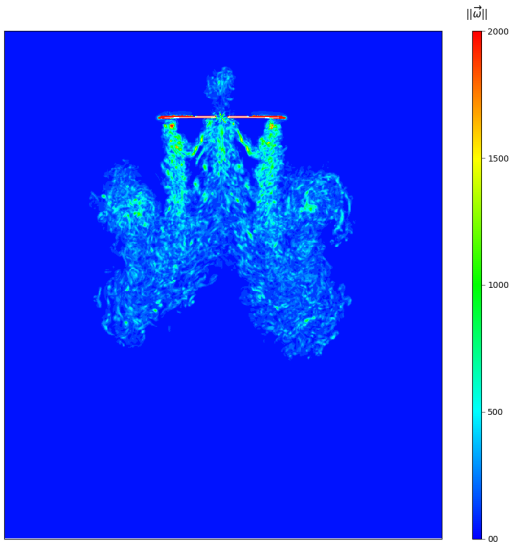

Figure 20: Vorticity for full LES in a slice at at the center of the blade.

The vorticity magnitude for the instantaneous field is displayed on a cut plane along the rotation axis (Figure 20), highlighting stronger vortices close the rotor than for the RANS/LES simulation, which are well-preserved and interacting downward after several revolutions.

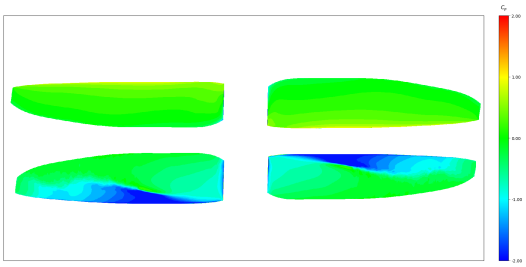

Figure 21: C_p map on the blade for the time averaged full LES.

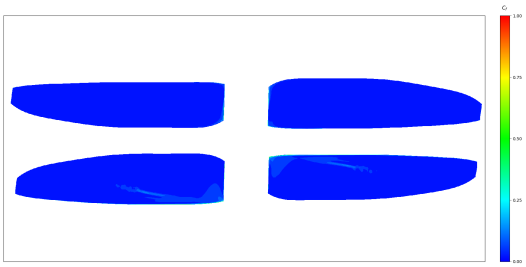

Figure 22: C_f map on the blade for the time averaged full LES.

6 RANS/LES and full LES Comparaison

From the Figures of Q criterion 18,9 and λ_2 criterion 19, 10 for LES simulation and their RANS/LES equivalent, some differences can be highlighted. The number of revolutions is smaller for the LES simulation, this is due to a computational time that is bigger than for the RANS/LES simulation. Then the turbulence on the blade can be seen and a vortex sheet has formed. This comes from the full resolution of the turbulence. The fact that the turbulence is much higher in this case is expected and it can be seen on the levels chosen for the isosurfaces.

Some differences can be clearly observed on the pressure coefficient distribution for the time averaged LES simulation in Figure 21 on the upper surface of the blade compared to the RANS/LES simulation shown in Figure 14. The friction coefficient is smaller than the one obtained with a RANS model.

During a revolution, the position of the main vortex core is tracked. Figures 23 and 24 compare the radial and vertical location of the vortex for the RANS/LES and full LES simulations.

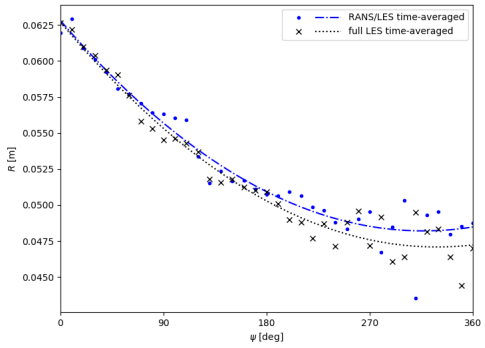

Figure 23: Radial position of the main vortex.

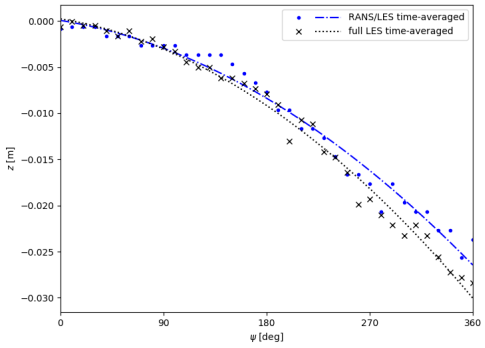

Figure 24: Vertical position of the principal vortex.

It can be seen in Figure 23 that the radial position of the main vortex is slightly different, less than a millimeter, for the time-averaged RANS/LES and full LES simulations. The vertical position of the main vortex shown on Figure 24 is also almost for the time-averaged results, less than $5mm$.

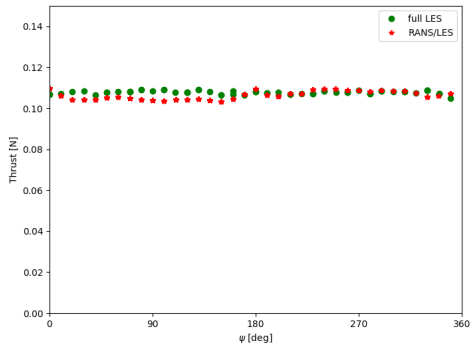

Figure 25: Thrust comparison after 9 revolutions.

The thrust is computed in the LES and RANS cases and is very similar for the two models as shown in Figure 25.

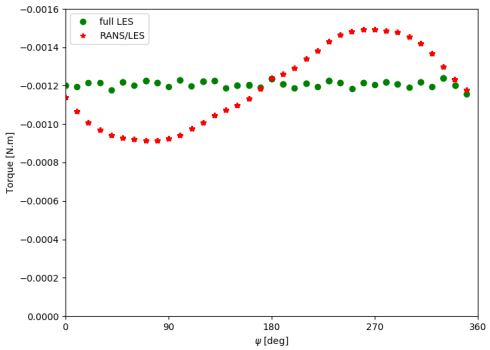

Figure 26: Torque comparison after 9 revolutions.

The torque value is oscillating for the RANS model. The average value of the large oscillations is approximately equal to the value of the LES model as shown in Figure 26. The LES computation results also in an oscillating value yet this is normal due to the fluctuating part in the quantities in the LES model.

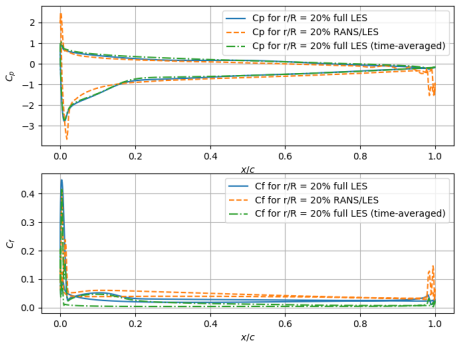

Figure 27: C_p and C_f at $r/R = 20\%$.

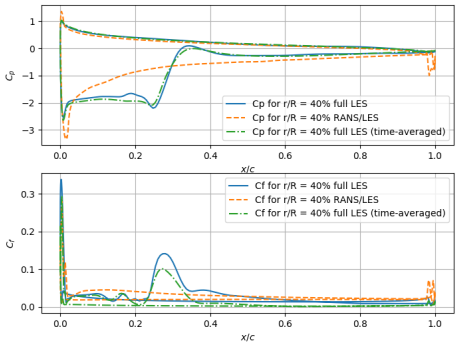

Figure 28: C_p and C_f at $r/R = 40\%$.

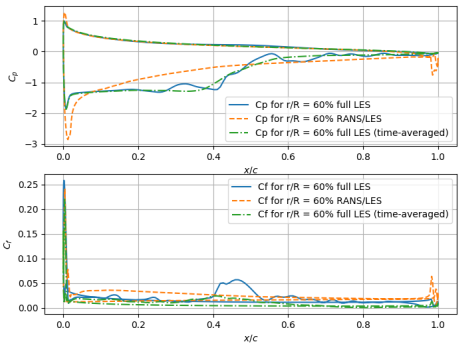

Figure 29: C_p and C_f at $r/R = 60\%$.

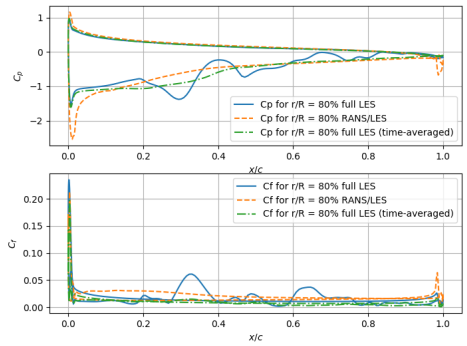

Figure 30: C_p and C_f at $r/R = 80\%$.

In Figures 27, 28, 29, and 30, the comparison between RANS/LES simulation, instantaneous LES simulation and time-averaged LES quantities for the pressure coefficient and friction coefficient are plotted. The pressure and friction values for the different radii are different at the leading edge.

Finally, the time averaged LES and the full LES give a different result than the RANS/LES for the upper surface. This highlights that the boundary layer is very different between the simulations for all radii.

To investigate this phenomenon the vorticity at $r/R = 40\%$, 60% and 80% are shown for the RANS/LES and time-averaged LES in Figures 31, 32, 33, 34, 35 and 36. As expected the RANS/LES results in a fully turbulent layer and the differences on the C_p and C_f curves can be seen.

For $r/R = 40\%$ the LES C_p curves shows a plateau before a sudden peak. On the vorticity Figure 31 the upper surface near the leading edge the boundary layer is laminar and a transition to a turbulent boundary layer is created when its being excited by the vortex shedding coming from the leading edge, this also results in the peak in the Cf value. For the RANS/LES simulation this vortex has been averaged by the model. At $r/R = 60\%$ the boundary layer becomes turbulent at around half the upper surface, on the Figure 33 we see the vortex shedding is exciting the turbulent layer but to a lesser extent than for $r/R = 40\%$ which creates a peak with a lower value. And finally for $r/R = 80\%$ the averaged LES is very close to the RANS/LES simulation because the boundary layer is not excited any more and is turbulent from the beginning.

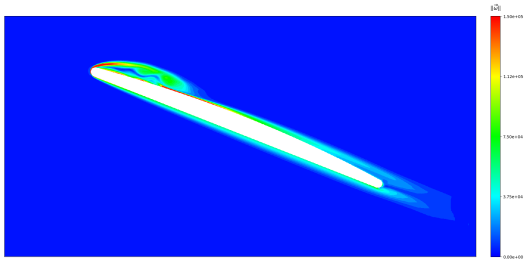

Figure 31: $||\overrightarrow{\omega}||$ at $r/R = 40\%$ for full LES simulation.

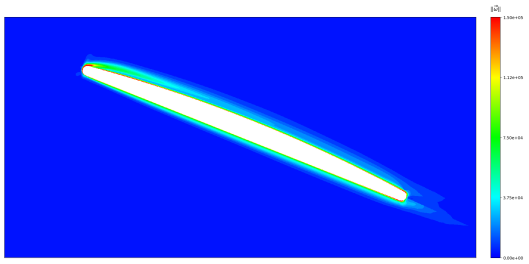

Figure 32: $||\overrightarrow{\omega}||$ at $r/R = 40\%$ for RANS/LES simulation.

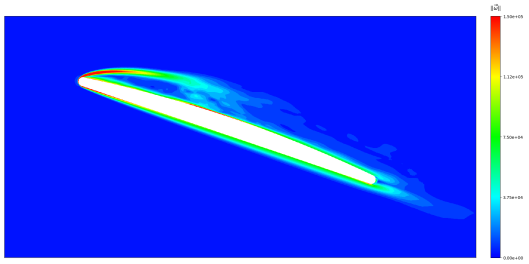

Figure 33: $||\overrightarrow{\omega}||$ at $r/R = 60\%$ for full LES simulation.

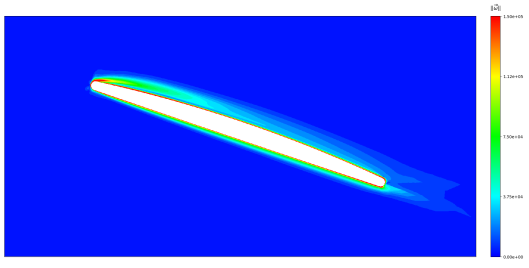

Figure 34: $||\overrightarrow{\omega}||$ at $r/R = 60\%$ for RANS/LES simulation.

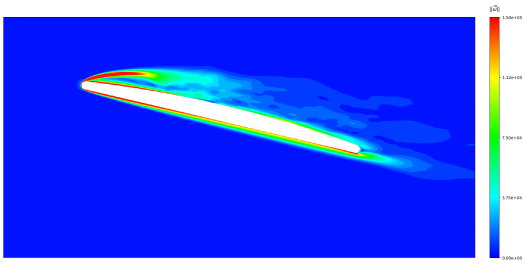

Figure 35: $||\vec{\omega}||$ at $r/R = 80\%$ for full LES simulation.

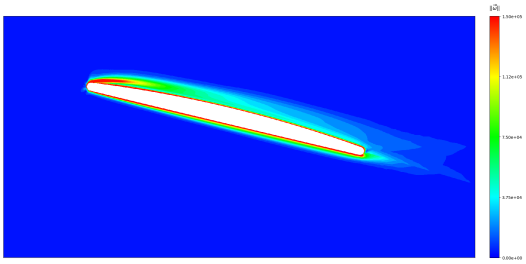

Figure 36: $||\vec{\omega}||$ at $r/R = 80\%$ for RANS/LES simulation.

7 Conclusions and outlook

A complete analysis of a drone propeller without hub has been provided and supported by different simulations that fuel a set of comparison. A complete description of the airfoil and of the propeller is also given to provide an open geometry that can be used for further comparisons.

All the quantities give a conclusion on the difference between an hybrid RANS/LES and full LES simulations. As expected the vorticity is more important for the full LES simulation which also generates a more resolved boundary layer since the curvilinear mesh is solved with a LES scheme. This creates a difference in the pressure and friction coefficient on the blade. Yet the value of thrust and torque generated by the propeller are close between the two simulations. This comes from the interaction of the wake because it is clear that the flow behavior near the wall is different between the two simulations. Although the vortex is less resolved for the RANS/LES simulation, its position across the revolution is quite identical for both simulations. Due to the heavy differences between the full LES and the RANS/LES simulations, further studies need to be done on the flow behavior for the full LES to describe the flow. Also the full LES simulation presented in this paper is not fully converged yet and with more revolutions and more time-average phases, the quantities can be different from what is presented here.

The computational time is 15 times bigger for the full LES simulation compared to the RANS/LES simulation. The next step of the study is to implement the hub to remove the recirculation due to its absence and to put four propellers to simulate the configuration of an entire drone. This implies a bigger domain for the whole simulation which is the bigger part of the mesh in terms of cell number.

References

[1] P. Ventura Diaz and S. Yoon. High-fidelity computational aerodynamics of multi-rotor unmanned aerial vehicles. *AIAA Aerospace Sciences Meeting, 2018*, 0(210059):1–22, 2018.

[2] P. R. Spalart and S. R. Allmaras. A One-Equation Turbulence Model For Aerodynamic Flows, 1994.

[3] J. P. Boris, F. F. Grinstein, E. S. Oran, and R. L. Kolbe. New insights into large eddy simulation. *Fluid Dynamics Research*, 10(4-6):199–228, 1992.

[4] M. S. Liou and C. J. Steffen. A new flux splitting scheme. *Journal of Computational Physics*, 107(1):23–39, 1993.

[5] J. R. Edwards and M. S. Liou. Low-diffusion Flux-splitting Methods For Flows at All Speeds. *AIAA Journal*, pages 261–271, 1997.

[6] I. Mary and P. Sagaut. Large eddy simulation of flow around an airfoil near stall. *AIAA Journal*, 40(6):1139–1145, 2002.

[7] S. Yoon and A. Jameson. Lu Implicit Scheme for High Speed Inlet Analysis. *AIAA Paper*, (April 1986), 1986.

[8] S. Péron and C. Benoit. Automatic off-body overset adaptive Cartesian mesh method based on an octree approach. *Journal of Computational Physics*, 232(1):153–173, 2013.

[9] J. Benek, J. Steger, and F. C. Dougherty. A flexible grid embedding technique with application to the Euler equations. In *6th Computational Fluid Dynamics Conference Danvers*, page 1944, 1983.

[10] C. Benoit, G. Jeanfaivre, and E. Canonne. Synthesis of ONERA Chimera method developed in the frame of CHANCE program. *31st European Rotorcraft Forum*, 2005:1–8, 2005.

[11] J C R Hunt, A. A. Wray, and P Moin. Eddies, streams, and convergence zones in turbulent flows. *Center for Turbulence Research, Proceedings of the Summer Program*, (1970):193–208, 1988.

[12] M. S. Chong, A. E. Perry, and B. J. Cantwell. A general classification of three-dimensional flow fields. *Physics of Fluids A*, 2(5):765–777, 1990.

[13] J. Jeong and F. Hussain. On the identification of a vortex. *Journal of Fluid Mechanics*, 285:69–94, 1995.

[14] C. Laurent, I. Mary, V. Gleize, A. Lerat, and D. Arnal. DNS database of a transitional separation bubble on a flat plate and application to RANS modeling validation. *Computers Fluids*, 61:21–30, may 2012.